Deep-Learning Approach to the Self-Piercing Riveting of Various Combinations of Steel and Aluminum Sheets

HYUN KYUNG KIM[1], **SEHYEOK OH**[1], **KEONG-HWAN CHO**[2], **DONG-HYUCK KAM**[2], **AND HYUNGSON KI**[1]

[1]Department of Mechanical Engineering, Ulsan National Institute of Science and Technology (UNIST), Ulsan 44919, South Korea
[2]Advanced Functional Technology Research and Development Department, Korea Institute of Industrial Technology, Incheon 21999, South Korea

Corresponding authors: Hyungson Ki (hski@unist.ac.kr) and Dong-Hyuck Kam (kamdong@kitech.re.kr)

ABSTRACT Deep-learning architectures were employed to simulate the self-piercing riveting process of steel and aluminum sheets and predict the cross-sectional joint shape with a zero head height. Four steels (SPRC440, SPFC590DP, GI780DP, SGAFC980Y) and three aluminum alloys (Al5052, Al5754, Al5083) were considered as the materials for the top and bottom sheets, respectively. The key objective was to consider the material properties of these metal sheets (Young's modulus, Poisson's ratio, and ultimate tensile strength) in a deep-learning framework. Two deep-learning models were considered: In the first model, the properties of the top and bottom sheets were adopted as the scalar inputs, and in the second model, the three properties were graphically assigned to the three channels of the input image. Both the models generated a segmentation image of the cross-section. To assess the accuracy of the predictions, the generated images were compared with ground truth images, and three key geometrical factors (interlock, bottom thickness, and effective length) were measured. The first and second models achieved prediction accuracies of 91.95% and 92.22%, respectively.

INDEX TERMS Self-piercing riveting, cross-sectional shape prediction, deep learning, segmentation map prediction, material properties.

I. INTRODUCTION

Self-piercing riveting (SPR) is an advanced process to realize the mechanical joining of two or more sheet metals by piercing a rivet into the sheets. As the rivet penetrates the top and bottom sheets, a mechanical interlock is formed between the two sheets. Because the process is performed under cold forming conditions, SPR has been widely implemented to join dissimilar materials such as aluminum alloys and steels, especially in automobile industries [1]. The SPR process exhibits many advantages over other conventional joining techniques such as welding in terms of pre-processing or energy requirements, quality of results, and environmental friendliness [2]. Notably, SPR can be used to join two dissimilar sheets in an inexpensive manner with a small energy consumption, and a high strength can be achieved.

To reduce the experimental efforts and optimize the process, it is desirable to perform simulations of the SPR

process prior to the actual processing. Several researchers have attempted to perform finite element analyses pertaining to the SPR process, focusing on the joining process, process optimization, and fatigue behavior [3]. Porcaro *et al.* [4] conducted the earliest 2D numerical simulations of the SPR process, based on the finite element method (FEM). To validate the simulation results, the force–deformation curves and deformed shapes were compared to the experimental results. Moreover, the authors investigated the behavior of the SPR joints under various quasi-static loading conditions by converting the 2D model for the riveting process to a 3D numerical model [5]. Both studies were conducted considering aluminum alloy 6060 of two different temper types. Bouchard *et al.* [6] simulated the 2D riveting process using finite element software, and compared the numerical results with experimentally obtained cross-section images. In addition, a structural analysis was conducted by simulating the shearing test considering the results of the riveting process. Furthermore, Atzeni *et al.* [7] used the FEM to predict the deformed shape, failure mechanism, and shear resistance of

The associate editor coordinating the review of this manuscript and approving it for publication was Jingang Jiang.

an SPR joint by simulating the joining process and tensile test of Al6082-T4 sheet metal. Similarly, Moraes *et al.* [8] attempted to simulate the SPR process for magnesium alloys by using a large-scale plasticity and damage model based on internal state variables and FEM to consider the complex physics phenomena occurring in the joining process. The numerical results of the final state were compared with the experimentally obtained cross-sections. Carandente *et al.* [9] proposed a 2D model based on a thermo-mechanical FEM to simulate the SPR process and investigated the effects of the change in the thermal and strain rate of substrate materials on the thermal softening and strain hardening. In most studies, the experimentally obtained and numerically simulated cross-sections were compared to evaluate the results, because, in general, the joint quality of the SPR can be determined by considering the geometrical factors of the cross-sectional shape such as the rivet flaring, bottom thickness, and effective length [10]. Haque *et al.* [11] proposed a simple model to determine the rivet flaring from the force–displacement curve, without cutting the SPR joint. Hönsch *et al.* [12] experimentally and numerically investigated the SPR process of aluminum alloy blanks with coated steel rivets. To evaluate the simulation results, geometrical factors of the cross-sections, such as the undercut and bottom thickness, were compared to the experimentally obtained values.

Recently, Oh *et al.* [13] proposed a deep-learning model to predict the cross-sectional shape from the input punch force of the SPR process, and the three key geometric factors in the cross-section were measured to assess the prediction quality. Deep-learning models offer several advantages over other simulation methods such as the FEM; specifically, deep-learning models do not require the implementation of any assumptions, and because these approaches are data-driven, all complex problems can be solved with sufficient data. The authors obtained predictions for CFRP-GA590DP and SPFC590DP-Al5052 combinations by using only the punch force as the input parameter. Because the characteristics of the materials used in the process were not considered as parameters, the prediction results were limited to the given material combination. In this regard, it is desirable to develop a model that can be used to predict the results considering the materials, to facilitate the use of novel materials in the SPR process.

Considering these aspects, in this study, based on the authors' previous work [13], two deep-learning models were developed, which could consider the material properties of the top and bottom sheet materials (steel and aluminum alloy, respectively) in a deep-learning framework and predict the cross-sectional joint shape for various sheet combinations. As the first model, the previously developed generative model (known as the scalar-to-seg model [13]), which was based on a convolution neural network (CNN) [14] and generative adversarial network (GAN) [15] with residual blocks [16] was adopted. However, in contrast to the previous model, which adopted the punch forces as the inputs,

the material properties of the top and bottom sheets were considered as the inputs. As the second model, the pix2pix model [17] was adopted and modified to predict the geometrical shape from the input image, containing not only the material properties of the top and bottom sheets but also those of the rivet. The two models were trained to learn the mapping from the material properties to a cross-sectional shape for a given material combination. Because the punch force was not an input parameter in these models, the models were designed to generate an optimal result in which the head height (gap between the rivet head and top sheet) was zero.

II. DATA PREPARATION
Figure 1 shows the schematics of the two deep-learning models adopted in this study. Both the models consider the material properties of the sheets as an input and have the same overall structure: the generator generates the cross-sectional image of the given materials, and the discriminator determines whether the given image is the generated image (fake) or ground truth image (real). The methods differ in terms of the type of input data and network structure. In the case of Model 1, a vector consisting of three material properties of the top and bottom sheets is input to the generator. In contrast, in the case of Model 2, an image in which the material properties are represented as values of the R, G, and B colors is input to the generator. The details on the inputs and network structures of the two models are explained in Sections III-A and B.

To obtain the ground truth data for the model, SPR experiments were conducted using 12 different combinations of steel and aluminum sheets. The list of materials and their properties are presented in Table 1 and 2. A C-type rivet and DZ type die were used for all combinations, and the corresponding geometric dimensions and shapes are shown in Figs. 2(a) and 2(b), respectively. Additional information regarding the rivet is presented in Table 3. The notations of the 12 combinations, referred to as the condition numbers in the paper, are presented in Table 4. The SPR process was conducted thrice for each combination, by using a hydraulic riveting machine (Rivset Gen2, BÖLLHOFF) with a pre-clamping force of 4 kN. The punch force for each combination was set such that the head height for the result was zero.

Using the optical microscopic (OM) images obtained by cutting the specimen after the SPR experiments, segmentation maps were prepared manually (see Fig. 2(c)) and used as the ground truth data of the models. As shown in Fig. 2(c), a segmentation map involved four classes (assigned to each channel of the image) representing the location of the rivet, top sheet, bottom sheet, and background with red, green, blue, and black colors, respectively. The three key geometrical factors of the cross-section, which are indicative of the quality of the SPR process, are shown in the segmentation map in Fig. 2(c). These factors, namely, the interlock (amount of rivet flaring), bottom thickness (distance between the rivet foot and bottom sheet), and effective length (amount of rivet pierced into the bottom sheet)
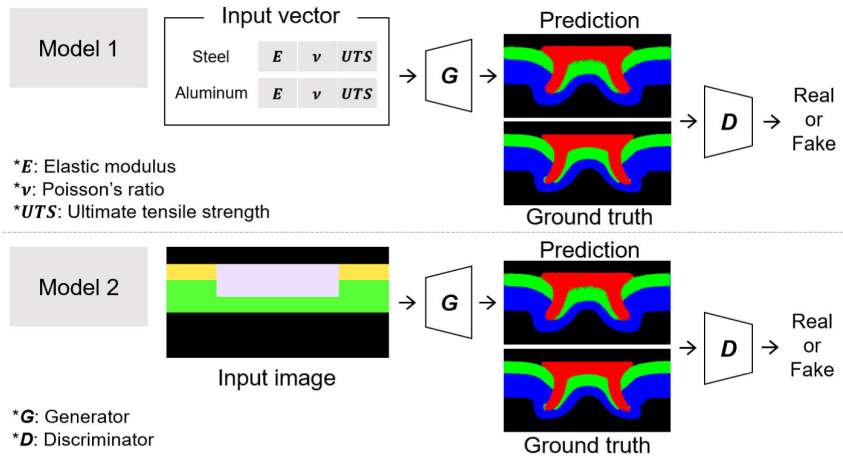
FIGURE 1. Data flow of two models used to predict the cross-sectional shape. The overall structures of Models 1 and 2 are similar, but they differ in the network structure of the generator and type of inputs.

TABLE 1. Properties of steel (top sheet) used in the SPR experiment.

Sheet material	Thickness	Elastic modulus	Poisson's ratio	Ultimate tensile strength
SPRC440				440 MPa
SPFC590DP	1 mm	205 GPa	0.3	590 MPa
GI780DP				780 MPa
SGAFC980Y				980 MPa

TABLE 2. Properties of the aluminum alloys (bottom sheet) used in the SPR experiment.

Sheet material	Thickness	Elastic modulus	Poisson's ratio	Ultimate tensile strength
Al5052				228 MPa
Al5754	2 mm	70.3 GPa	0.33	305 MPa
Al5083				315 MPa
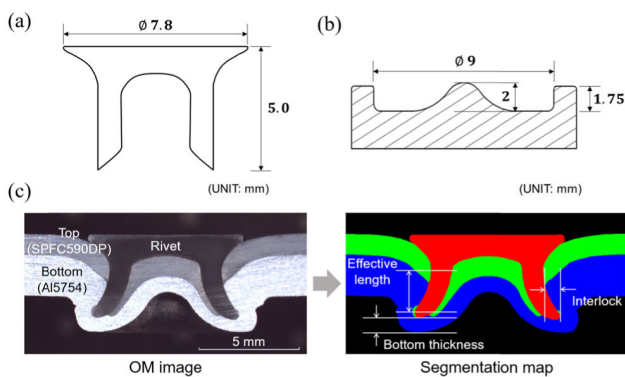
FIGURE 2. Dimensions of (a) rivet and (b) die used in the SPR experiment. The segmentation map generated from the OM image is shown in (c), and the key geometrical factors that indicate the SPR joint quality are shown.

were measured to assess the prediction quality, as described in Section IV.

As indicated in Fig. 1 and mentioned previously, Model 2 requires an image input. To obtain the input image, the three considered properties of the materials used in the SPR process, specifically, the elastic modulus, Poisson's ratio, and ultimate tensile strength, were normalized and assigned as R, G, and B channels, respectively. Figure 3 shows two sample input images corresponding to different material combinations. Normalized values of elastic modulus, Poisson's ratio, and ultimate tensile strength are written in red, green, and blue, respectively. Each value indicates a pixel value of the R, G, and B channel of an image. As shown, the colors of the top and bottom sheets in two images are different as different materials were used. Comparing the left and right images, only the B values of steel sheets are different because only ultimate tensile strength is different for the steels (see Table 1). Moreover, the locations of the materials were set considering the actual states of specimens before the process. The colors of the rivet and top and bottom sheets appeared different as different materials were used, as shown

TABLE 3. Properties of the rivet used in the SPR experiment.

Material	Type	Coating	Hardness (HV)
Boron steel (BÖLLHOFF)	C-type	Almac	480 $\pm$ 30

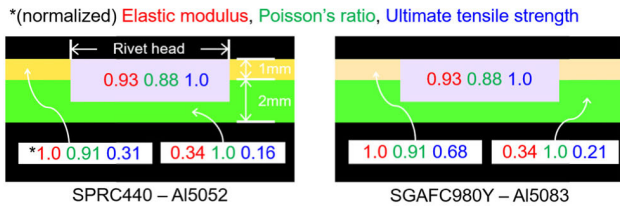| Elastic modulus	Poisson's ratio	Ultimate tensile strength
190 GPa	0.29	1440 MPa

FIGURE 3. Input images for Model 2. Three material properties (elastic modulus, Poisson's ratio, and tensile strength) of the rivet, top and bottom sheets are considered as R, G, B channels and the corresponding values (normalized) are written in red, green, and blue color, respectively, in above images. In other words, the color of a material represents material properties (e.g., the left and right images have different colors as they correspond to different combinations of steel and aluminum materials, as indicated below the images). The locations of the materials are set considering the actual states before the process.

TABLE 4. Notations of the 12 combinations of steel–aluminum sheets used in the SPR experiment. (referred to as the condition numbers).

Top sheet \ Bottom sheet	Al5052	Al5754	Al5083
SPRC440	(1)	(2)	(3)
SPFC590DP	(4)	(5)	(6)
GI780DP	(7)	(8)	(9)
SGAFC980Y	(10)	(11)	(12)

in Fig. 3. Furthermore, the properties of the rivet were considered as parameters in the input image along with the top and bottom sheets, which allowed the model to take into account any change in the material of the rivet as well as the top and bottom sheets.

III. DEEP-LEARNING MODELS

A. MODEL 1: USING MATERIAL PROPERTIES AS THE SCALAR INPUTS

Figure 4 shows the structure of Model 1 to predict the cross-sectional shape of the specimen after the SPR process. A previously proposed generative model (scalar-to-seg generator) [13] was adopted, which was based on the CNN and conditional GAN (cGAN) [18] architecture with residual blocks. As shown in Fig. 4, Model 1 involved a generator and discriminator. The generator generated the cross-sectional image from the condition vector and random noise vector, and the discriminator determined whether the image was real (ground truth) or fake (prediction). This type of GAN model has been widely used in image processing applications, for instance, to solve image generation problems. The output image of the generator, known as the segmentation map, consisted of four channels that represented the rivet, top

sheet, bottom sheet, and background class, and each pixel value (between 0 and 1) indicated the probability that the pixel belonged to each class. The objective functions for the generator and discriminator were as follows:

$$\min_{D} V(D) = \frac{1}{2}\mathbb{E}_{x,c}[(D(x,c)-1)^2] + \frac{1}{2}\mathbb{E}_{c,z}[(D(G(c,z),c))^2] \quad (1)$$

$$\min_{G} V(G) = \frac{1}{2}\mathbb{E}_{c,z}[(D(G(c,z),c)-1)^2] + \lambda\mathbb{E}_{x,c,z} \times [-x\ln G(c,z)] \quad (2)$$

To enhance the learning stability, the least-squares GAN loss (LSGAN) [19] and extra cost function (the right most term in (2)) were used. Furthermore, residual connections [16], [20] were implemented, as shown in Fig. 4, to enable effective learning with deeper layers. More details regarding the adopted model can be found in [13].

Notably, unlike the previous model [13], a condition vector composed of the material properties of the top and bottom sheet materials, was used as the input of the generator instead of the scalar punch forces. Because the punch force was not an input parameter, it was set such that the head height was zero. The materials of only the top and bottom sheets were considered as the inputs because the rivet materials did not change. The elastic modulus, Poisson's ratio, and ultimate tensile strength were considered as the material properties, as, in general, these properties are representative of a material. Therefore, the condition vector involved six scalar values (with the top and bottom materials corresponding to three values) after the properties were normalized to range between -1 and 1. Additionally, the ratio of the number of feature maps for the random noise vector to those of the condition vector was set as 3:1 based on trial and error (the value was 10:1 in the previous work [13]); the corresponding numbers of channels of the random noise vector and condition vector after the linear layer (project and reshape) were 768 and 256, respectively. The influence of the input parameters on the training increased owing to the increase in the number of components of the input from 1 (only the scalar punch force was considered as the input in [13]) to 6 (vector consisting of six scalar values). Although models with instance normalization [21] and full pre-activation [22] were tested, superior results were not achieved. In addition, we attempted to enhance the quality of the resulting images by adding the feature mapping loss utilized in the pix2pixHD model [23] to the objective functions; however, the impact on the results was negligible. The deep-learning source codes were implemented using Python and TensorFlow.
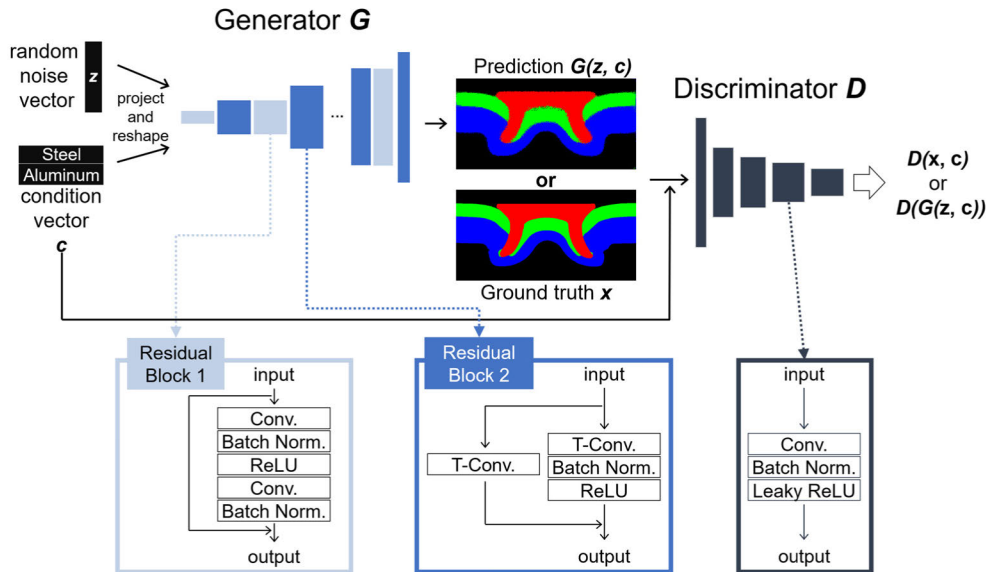
FIGURE 4. Structure of Model 1. The model consists of a convolutional generator and discriminator. The generator features two types of residual blocks, as shown in the bottom of the image. The condition vector, which consists of the three material properties of the top and bottom sheets, is input to the generator, with a random noise vector.

B. MODEL 2: GRAPHICAL IMPLEMENTATION OF MATERIAL PROPERTIES

Figure 5 illustrates the structure of Model 2, used to predict the cross-sectional shape of the specimen after the SPR processing. By adopting the pix2pix architecture [17], which is based on cGAN, the generator generated a segmentation map as an output image, similar to that of Model 1, from an input image. However, in contrast to Model 1, the input was an image and not a vector, and thus, the prediction task corresponded to image-to-image generation. The generator had an encoder–decoder structure based on the U-Net [24] architecture, in which the skip-connection was well utilized to recover the lost information during the encoding process. More detailed information regarding the model can be found in [17].

As shown in Fig. 5, an image, representing the material properties, location of the rivet and top and bottom sheet as colors (as explained in Section II), was input to the generator. The segmentation map was generated through the decoding layers by using the information of the given material extracted through the encoding layers. Note that, in Model 2, the rivet material was also considered, so rivets made of different materials can be simulated.

In a previous work [17], the authors ignored the effect of the random noise vectors (z) in the pix2pix model and did not report on any effective solution to obtain a highly non-deterministic output image. However, we attempted to utilize random noise vectors in this study to ensure a small amount of stochasticity to take into account the repetition of the experiments. To fully exploit the random noise vector by preventing it from being ignored through encoding layers, we added the vector in the bottleneck layer of the generator; consequently, sufficient non-deterministic results were obtained to express the repetitions. In addition, a softmax

layer was used as the last activation layer of the generator in Model 2 instead of the tanh layer. Thus, the output image was a segmentation map composed of four classes, in which each pixel took 0 or 1 values on each class. Instead of the L1 loss, CEE was used as an extra cost function of the generator, and the loss functions of Model 2 were the same as those of Model 1 (written in (1) and (2)).

C. TRAINING DETAILS

In both the models, the learning proceeded in the same manner, with the same data set. The training was performed in two sessions. Figure 6 shows the data set for each session, in which the 12 combinations of top and bottom sheets were divided into training data and test data. In session 1, among the three aluminum sheets (Al5052, Al5754, Al5083), one aluminum sheet (Al5754) was fixed as the bottom sheet as the test data and the combinations of the other two aluminum and steel sheets were used for training. In this scenario, the prediction was conducted on the aluminum sheet for which the model was not trained, corresponding to a prediction on a new material. Similarly, one steel sheet (SPFC590DP) was fixed as the top sheet as the test data, and the others were used for training. The training images were augmented by weak shear transformation ($\times 50$) and left-right flip ($\times 2$). Consequently, 2400 and 2700 images were used in each training session (considering the three repetitions of the experiments for each combination). The learning rate, lambda of L2 regularization, and batch size were determined using the random search method as $10^{-6.8} \approx 1.58 \times 10^{-7}$, 10^{-5}, and 12, respectively, for Model 1. For Model 2, the corresponding values were 3×10^{-7}, 10^{-4}, and 12. The models were trained using TITAN RTX GPUs, and the Adam [25] optimizer was adopted. To validate the model, early stopping regularization was implemented: In general, as the training progresses,
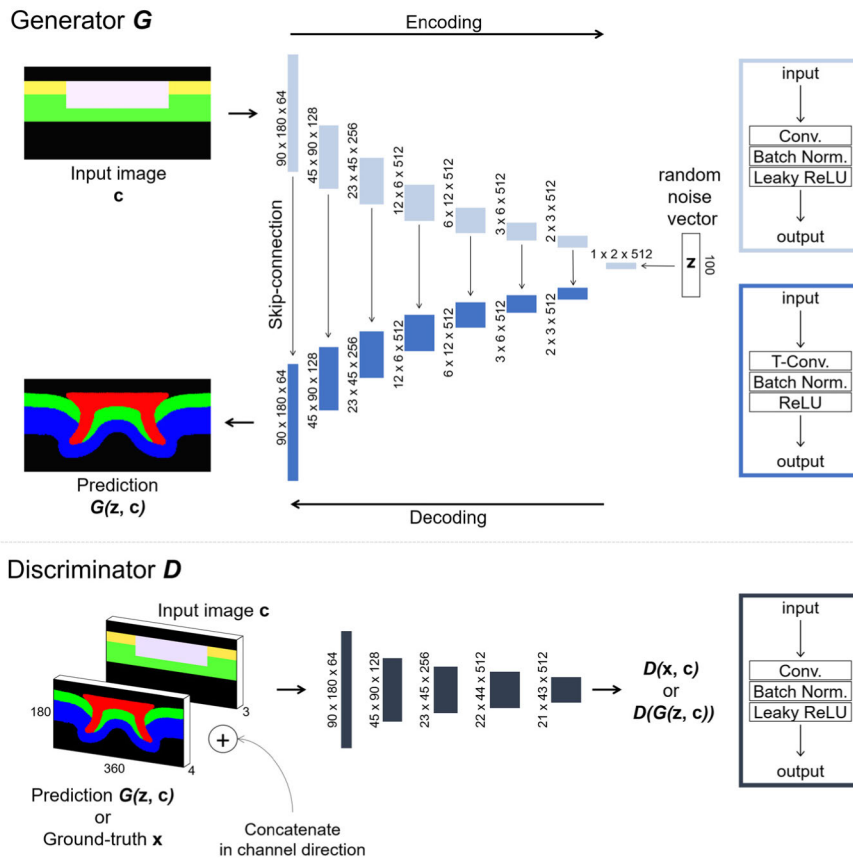
FIGURE 5. Structure of Model 2. The model consists of a U-Net based generator and convolutional discriminator. An image containing information regarding the material properties is input to the generator that involves a skip-connection. A random noise vector is added to the bottleneck layer to enable the repetitions of the experiment. Each block in the right side of the figure, surrounded by a thick line, represents the network structure inside the blocks filled in with the same color.
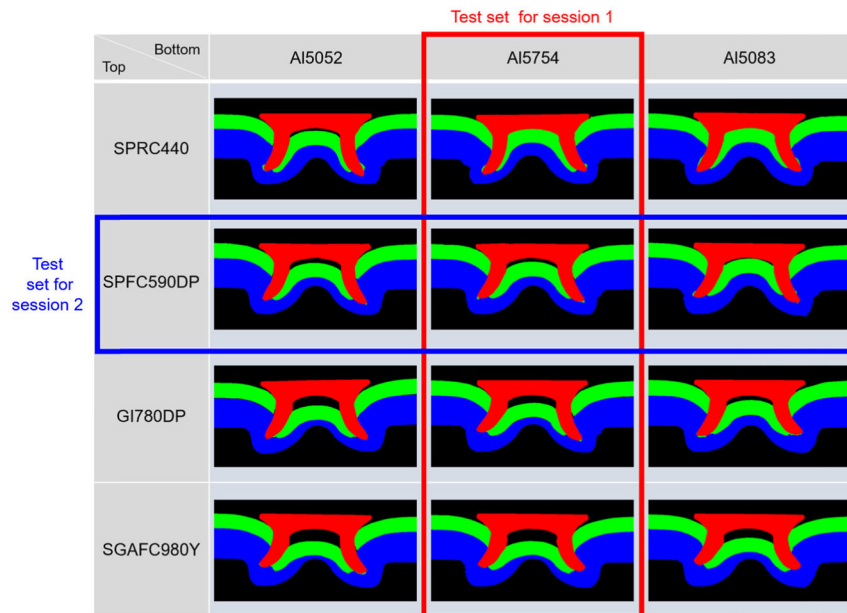
FIGURE 6. Visual representations of the training and test data for sessions 1 and 2. In both the sessions, one of the top or bottom sheets was selected as the test data, and the other sheets were considered for training. All the images correspond to the ground truth data.
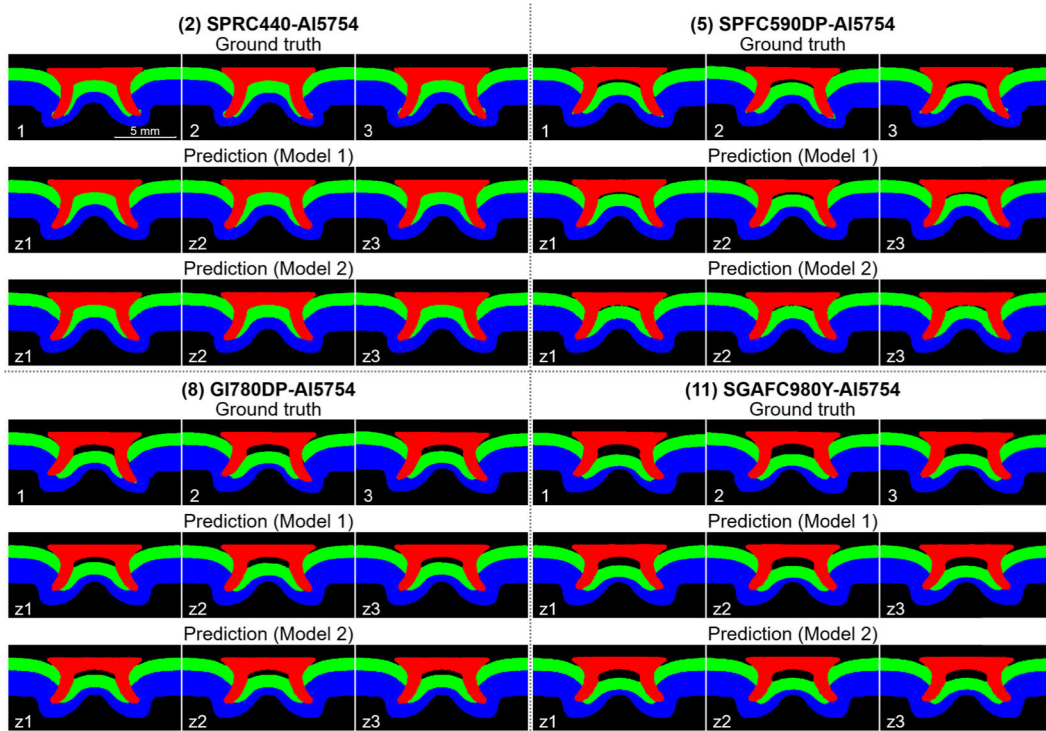
FIGURE 7. Comparison of prediction results of Models 1 and 2 with the ground truth images. In session 1, the aluminum (bottom sheet) type was Al5754, and only type of steel (top sheet) was changed. As the condition number increased, the ultimate tensile strength of the steel sheet increased. The bottom-left number marked in the ground truth images indicates the number of repeated experiment. The labels marked in the predicted images such as z1, z2, and z3 indicate different random noise vectors (z).
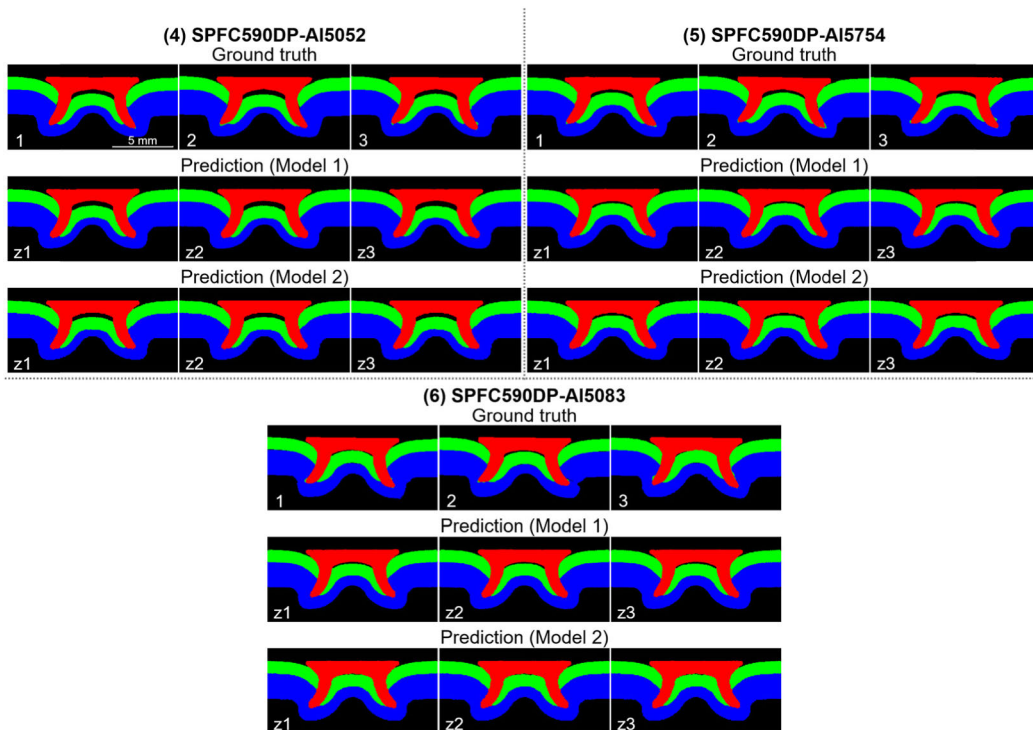
FIGURE 8. Comparison of prediction results of Models 1 and 2 with ground truth images. For session 2, the type of steel (top sheet) was fixed as SPFC590DP, and only the type of aluminum (bottom sheet) was changed. As the condition number increased, the ultimate tensile strength of the aluminum sheet increased. The bottom-left number marked in the ground truth images indicates the number of repeated experiment. The labels marked in the predicted images such as z1, z2, and z3 indicate different random noise vectors (z).

the test data loss initially decreases and starts to increase at a certain point, while the training data loss continues to decrease. This phenomenon indicates that the model is overfit to the training data; to avoid overfitting, the model should be stopped at the point at which the test data loss is minimized.

IV. RESULT AND DISCUSSION

The test results (generated images after training) of the two models are shown in Figs. 7 and 8. In both figures, the ground truth images are represented in the first row of each condition, and the images predicted using Models 1 and 2 are presented in the second and third rows, respectively. Three images were generated using different z to express the experimental trials for each condition. Therefore, the three columns of each condition correspond to the repeated experiments for the ground truth images and the use of different z for the predicted images.

Figure 7 shows the results of session 1. As the condition number changed from (2) to (5) to (8) to (11), the ultimate tensile strength of the steel sheet increased. Moreover, the size of the cavity (empty space between the rivet and top sheet) in the ground truth images increased with the increasing tensile strength of the steel sheet. In other words, a larger cavity appeared when a higher strength steel was used as the top sheet. The comparison of the ground truth data and prediction results of Models 1 and 2 shown in Fig. 7 indicates that both the models achieved satisfactory predictions for session 1 for all test conditions in terms of the change in the cavity in each condition.

The results of session 2 are shown in Fig. 8. The test was performed with three combinations of the top and bottom sheets. The steel (top sheet) was fixed for the test data, and three types of aluminum (bottom sheet) were considered. Similar to the results for session 1, as the condition number changed from (4) to (6), the ultimate strength of the aluminum sheet increased; however, in contrast to the images shown in Fig. 7, the size of the cavity in the ground truth images decreased even though the same steel was used as a top sheet for all the test conditions. This phenomenon occurred because the rivet was located in a relatively higher position owing to the smaller amount of rivet pierced into the bottom sheet when aluminum with a higher strength was used as bottom sheet. The comparison of the predicted images with the ground truth images in Fig. 8 shows that both the models well predicted the cross-sectional shape in all the test conditions in terms of the cavity size.

To quantitatively assess the results, the three key geometry factors shown in Fig. 2(c) were measured. The measurements were obtained for both the left and right sides of the images, and the values were averaged. The measurement results of the interlock, bottom thickness, and effective length were compared with those of the ground truth, as shown in Figs. 9, 10, and 11, respectively. Indexes (a) and (b) in the figures represent the results of sessions 1 and 2, respectively. The ultimate tensile strength of steel or aluminum increased along the x-axis in all the graphs.
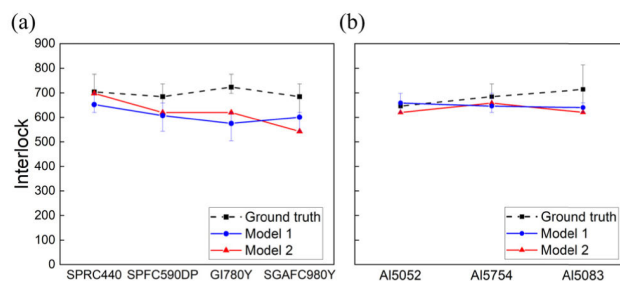
FIGURE 9. Measurement of the interlock for the prediction results and ground-truths. The black, blue, and red lines represent the ground-truths and predictions of Models 1 and 2, respectively. For (a), the aluminum (bottom sheet) type was fixed as Al5754, and the x-axis indicates the change in the steel materials (top sheet). For (b), the steel (top sheet) was fixed as SPFC590DP, and the x-axis indicates the change in the aluminum materials (bottom sheet).
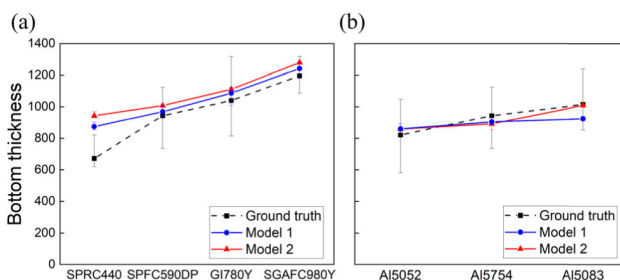
FIGURE 10. Measurement of the bottom thickness for the prediction results and ground-truths. The black, blue, and red lines represent the ground-truths and predictions of Models 1 and 2, respectively. For (a), the aluminum (bottom sheet) type was fixed as Al5754, and the x-axis indicates the change in the steel materials (top sheet). For (b), the steel (top sheet) was fixed as SPFC590DP, and the x-axis indicates the change in the aluminum materials (bottom sheet).
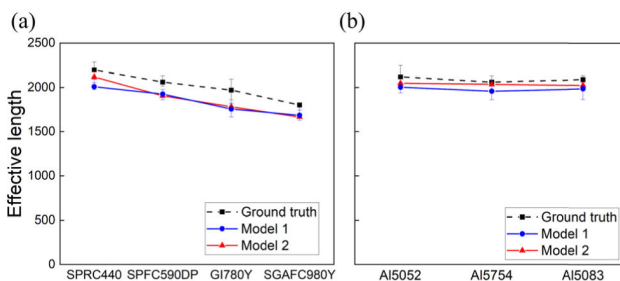
FIGURE 11. Measurement of the effective length for the prediction results and ground-truths. The black, blue, and red lines represent the ground-truths and predictions of Models 1 and 2, respectively. For (a), the aluminum (bottom sheet) type was fixed as Al5754, and the x-axis indicates the change in the steel materials (top sheet). For (b), the steel (top sheet) was fixed as SPFC590DP, and the x-axis indicates the change in the aluminum materials (bottom sheet).

As shown in Fig. 10, the bottom thickness increased along the x-axis for the ground truth data in both sessions, and the prediction results of Models 1 and 2 exhibited the same tendency of the ground truth data. Thus, the bottom thickness was influenced by the change in the aluminum and steel sheets.

However, the effective length decreased along the x-axis only in session 1, and no conspicuous tendency was observed in session 2, as shown in Fig. 11(b). In other words,

the effective length was influenced only by the change in steel sheets and not by that in the aluminum sheets. As in the case of the bottom thickness, the prediction results of both models followed the tendency of the ground truth data in both sessions. Therefore, both the models were adequately trained to learn the relationship between the cross-sectional shape after SPR processing and material combinations.

For the interlock, the prediction results of the two models did not follow the tendency of the ground truth data in both the sessions (see Fig. 9), likely because the interlock did not exhibit a significant increasing or decreasing trend in the case of both the steel and aluminum materials considering the total ground truth data (including training and test data).

Tables 5 and 6 present the percentage accuracies of the interlock, bottom thickness, and effective length for Models 1 and 2, respectively. For Model 1, the accuracy for sessions 1 and 2 was 89.60% and 94.30%, respectively; the total averaged accuracy was 91.95%. For Model 2, the accuracy for sessions 1 and 2 was 88.80% and 95.63%, respectively; the total averaged accuracy was 92.22%. Overall, both models exhibited a high performance to predict the cross-sectional shape after SPR processing, although the total accuracy for Model 2 was slightly higher than that for Model 1.

TABLE 5. Percentage accuracies for the interlock, bottom thickness, and effective length for the results of Model 1.

Session 1					
Condition number	(2)	(5)	(8)	(11)	avg
Interlock (%)	92.66	88.71	79.46	87.74	87.14
Bottom thickness (%)	70.12	97.30	95.52	96.06	89.75
Effective length (%)	91.47	93.42	89.18	93.55	91.90
				Total avg	89.60%

Session 2				
Condition number	(4)	(5)	(6)	avg
Interlock (%)	98.00	94.34	89.61	93.98
Bottom thickness (%)	95.28	95.87	91.04	94.06
Effective length (%)	94.51	94.98	95.05	94.85
			Total avg	94.30%

TABLE 6. Percentage accuracies for the interlock, bottom thickness and effective length for the results of Model 2.

Session 1					
Condition number	(2)	(5)	(8)	(11)	avg
Interlock (%)	99.08	90.57	85.71	79.25	88.65
Bottom thickness (%)	59.82	93.15	93.17	92.91	84.76
Effective length (%)	96.47	92.48	90.49	92.47	92.98
				Total avg	88.80%

Session 2				
Condition number	(4)	(5)	(6)	avg
Interlock (%)	96.00	96.23	86.89	93.04
Bottom thickness (%)	95.35	94.52	99.36	96.41
Effective length (%)	96.65	98.75	96.90	97.43
			Total avg	95.63%

These prediction results demonstrate the advantage of using deep-learning models in addressing SPR process problems instead of conventional simulation methods. Notably, the cross-sectional shape after the SPR processing of

any metallic material can be predicted by using various deep-learning models if the material properties are known. In this study, to simplify the task, the change in the rivet material was not considered; however, any change in the rivet material can be considered by simply adding the material properties of the rivet along with those of the top and bottom sheets.

V. CONCLUSION
Two types of deep-learning model were applied to predict the cross-sectional shape of specimen after SPR processing, by taking into account the material properties. Four steels (SPRC440, SPFC590DP, GI780DP, SGAFC980Y) and three aluminum alloys (Al5052, Al5754, Al5083) were used as materials for the top and bottom sheet, respectively, leading to 12 combinations of steel and aluminum sheets. The key contributions of this work can be summarized as follows:

- The two models were based on a GAN, which consisted of a generator and discriminator and generated segmentation (cross-sectional) images from the material properties of the considered combinations. The first model adopted a CNN with residual blocks and used a vector including the material properties of the top and bottom sheets as the input to the generator. In the second model, based on the pix2pix architecture, an image in which the material properties of the top and bottom sheets and rivet were represented as colors was input to the generator.

- The training for both models was performed over two sessions. In both the sessions, the combinations of materials not used in training were used as testing data to verify the predictive ability of the model for new materials.

- The key geometrical factors for the cross-section, specifically, the interlock, bottom thickness, and effective length, were measured to assess the quality of prediction. The corresponding accuracies were 89.60% and 94.30% for Model 1 and 88.80% and 95.63% for Model 2. The total averaged accuracies for Models 1 and 2 were 91.95% and 92.22%, respectively.

- The geometrical shape of the SPR processing for any metallic material can be predicted using a deep-learning model if the material properties are known; in this manner, the time spent on establishing the SPR process for new materials can be reduced.

REFERENCES
[1] A. Luo, T. Lee, and J. Carter, "Self-pierce riveting of magnesium to aluminum alloys," *SAE Int. J. Mater. Manuf.*, vol. 4, no. 1, pp. 158–165, Apr. 2011.

[2] D. Li, A. Chrysanthou, I. Patel, and G. Williams, "Self-piercing riveting— A review," *Int. J. Adv. Manuf. Technol.*, vol. 92, nos. 5–8, pp. 1777–1824, Sep. 2017, doi: 10.1007/s00170-017-0156-x.

[3] X. He, F. Gu, and A. Ball, "Recent development in finite element analysis of self-piercing riveted joints," *Int. J. Adv. Manuf. Technol.*, vol. 58, nos. 5–8, pp. 643–649, Jan. 2012, doi: 10.1007/s00170-011-3414-3.

[4] R. Porcaro, A. G. Hanssen, M. Langseth, and A. Aalberg, "Self-piercing riveting process: An experimental and numerical investigation," *J. Mater. Process. Technol.*, vol. 171, no. 1, pp. 10–20, Jan. 2006, doi: 10.1016/j.jmatprotec.2005.05.048.

[5] R. Porcaro, A. G. Hanssen, M. Langseth, and A. Aalberg, "The behaviour of a self-piercing riveted connection under quasi-static loading conditions," *Int. J. Solids Struct.*, vol. 43, no. 17, pp. 5110–5131, Aug. 2006, doi: 10.1016/j.ijsolstr.2005.10.006.

[6] P. O. Bouchard, T. Laurent, and L. Tollier, "Numerical modeling of self-pierce riveting—From riveting process modeling down to structural analysis," *J. Mater. Process. Technol.*, vol. 202, nos. 1–3, pp. 290–300, Jun. 2008, doi: 10.1016/j.jmatprotec.2007.08.077.

[7] E. Atzeni, R. Ippolito, and L. Settineri, "Experimental and numerical appraisal of self-piercing riveting," *CIRP Ann.*, vol. 58, no. 1, pp. 17–20, 2009, doi: 10.1016/j.cirp.2009.03.081.

[8] J. F. C. Moraes, J. B. Jordon, and D. J. Bammann, "Finite element analysis of self-pierce riveting in magnesium alloys sheets," *J. Eng. Mater. Technol.*, vol. 137, no. 2, Apr. 2015, Art. no. 021002, doi: 10.1115/1.4029032.

[9] M. Carandente, R. J. Dashwood, I. G. Masters, and L. Han, "Improvements in numerical simulation of the SPR process using a thermo-mechanical finite element analysis," *J. Mater. Process. Technol.*, vol. 236, pp. 148–161, Oct. 2016, doi: 10.1016/j.jmatprotec.2016.05.001.

[10] R. Haque, "Quality of self-piercing riveting (SPR) joints from cross-sectional perspective: A review," *Arch. Civil Mech. Eng.*, vol. 18, no. 1, pp. 83–93, Jan. 2018, doi: 10.1016/j.acme.2017.06.003.

[11] R. Haque, N. S. Williams, S. E. Blacket, and Y. Durandet, "A simple but effective model for characterizing SPR joints in steel sheet," *J. Mater. Process. Technol.*, vol. 223, pp. 225–231, Sep. 2015.

[12] F. Hönsch, J. Domitner, C. Sommitsch, B. Götzinger, and M. Kölz, "Numerical simulation and experimental validation of self-piercing riveting (SPR) of 6xxx aluminium alloys for automotive applications," *J. Phys., Conf. Ser.*, vol. 1063, no. 1, p. 12081, 2018.

[13] S. Oh, H. K. Kim, T.-E. Jeong, D.-H. Kam, and H. Ki, "Deep-learning-based predictive architectures for self-piercing riveting process," *IEEE Access*, vol. 8, pp. 116254–116267, 2020, doi: 10.1109/Access.2020.3004337.

[14] Y. Lecun, L. Bottou, Y. Bengio, and P. Haffner, "Gradient-based learning applied to document recognition," *Proc. IEEE*, vol. 86, no. 11, pp. 2278–2324, Nov. 1998, doi: 10.1109/5.726791.

[15] I. Goodfellow, J. Pouget-Abadie, M. Mirza, B. Xu, D. Warde-Farley, S. Ozair, A. Courville, and Y. Bengio, "Generative adversarial nets," in *Proc. Adv. Neural Inf. Process. Syst.*, 2014, pp. 2672–2680.

[16] K. He, X. Zhang, S. Ren, and J. Sun, "Deep residual learning for image recognition," in *Proc. IEEE Conf. Comput. Vis. Pattern Recognit. (CVPR)*, Jun. 2016, pp. 770–778.

[17] P. Isola, J.-Y. Zhu, T. Zhou, and A. A. Efros, "Image-to-image translation with conditional adversarial networks," in *Proc. IEEE Conf. Comput. Vis. Pattern Recognit. (CVPR)*, Jul. 2017, pp. 1125–1134.

[18] M. Mirza and S. Osindero, "Conditional generative adversarial nets," 2014, *arXiv:1411.1784*. [Online]. Available: http://arxiv.org/abs/1411.1784

[19] X. Mao, Q. Li, H. Xie, R. Y. K. Lau, Z. Wang, and S. P. Smolley, "Least squares generative adversarial networks," in *Proc. IEEE Int. Conf. Comput. Vis. (ICCV)*, Oct. 2017, pp. 2794–2802.

[20] S. Gross and M. Wilber. (2016). *Training and Investigating Residual Nets*. [Online]. Available: http://torch.ch/blog/2016/02/04/resnets.html

[21] D. Ulyanov, A. Vedaldi, and V. Lempitsky, "Instance normalization: The missing ingredient for fast stylization," 2016, *arXiv:1607.08022*. [Online]. Available: http://arxiv.org/abs/1607.08022

[22] K. He, X. Zhang, S. Ren, and J. Sun, "Identity mappings in deep residual networks," in *Proc. Eur. Conf. Comput. Vis.* Cham, Switzerland: Springer, 2016, pp. 630–645.

[23] T.-C. Wang, M.-Y. Liu, J.-Y. Zhu, A. Tao, J. Kautz, and B. Catanzaro, "High-resolution image synthesis and semantic manipulation with conditional GANs," in *Proc. IEEE/CVF Conf. Comput. Vis. Pattern Recognit.*, Jun. 2018, pp. 8798–8807.

[24] O. Ronneberger, P. Fischer, and T. Brox, "U-Net: Convolutional networks for biomedical image segmentation," in *Proc. Int. Conf. Med. Image Comput. Comput.-Assist. Intervent.* Cham, Switzerland: Springer, 2015, pp. 234–241.

[25] D. P. Kingma and J. Ba, "Adam: A method for stochastic optimization," 2014, *arXiv:1412.6980*. [Online]. Available: http://arxiv.org/abs/1412.6980

HYUN KYUNG KIM received the B.S. degree in mechanical engineering from the Ulsan National Institute of Science and Technology (UNIST), Ulsan, South Korea, in 2020, where she is currently pursuing the joint M.S. and Ph.D. degrees in mechanical engineering. Her research interests include application of deep learning in laser processing and mechanical engineering.

SEHYEOK OH received the B.S. and Ph.D. degrees in mechanical engineering from the Ulsan National Institute of Science and Technology (UNIST), Ulsan, South Korea, in 2014 and 2020, respectively. He is currently a Postdoctoral Researcher in mechanical engineering at UNIST. His research interests include application of deep learning to the laser materials processing and mechanical problems, such as mechanical deformation, self-piercing riveting, particle image velocimetry, and industrial application of high-power lasers, such as laser welding, laser cutting, and laser transformation hardening.

KEONG-HWAN CHO received the B.S. degree in mechanical engineering from Myoungji University, Yongin, South Korea, in 2020. He is currently pursuing the M.S. degree with the Department of Mechanical Design Engineering, Hanyang University, Gyeonggi-do, South Korea. He is a Research Assistant with the Advanced Functional Technology Research and Development Department, Korea Institute of Industrial Technology (KITECH). His research interests include the mechanical joining of dissimilar materials and laser surface treatment to improve the strength of adhesive bonding.

DONG-HYUCK KAM received the B.S. degree in mechanical engineering from the Pohang University of Science and Technology, Pohang, South Korea, in 2003, and the M.S.E and Ph.D. degrees in mechanical engineering from the University of Michigan, Ann Arbor, USA, in 2005 and 2009, respectively.

From 2011 to 2015, he was a Senior Engineer with Samsung Electronics Company, Ltd. Since 2015, he has been the Principal Researcher with the Joining Research and Development Group, Korea Institute of Industrial Technology (KITECH). His research interests include the mechanical joining of dissimilar materials, hybrid welding of zinc coated steel, laser-based joining technologies for CFRP-metal, 3D metal deposition with wire feeding, and laser material processing.

HYUNGSON KI received the B.S. degree in mechanical engineering from the Pohang University of Science and Technology (POSTECH), South Korea, in 1996, and the M.S. and Ph.D. degrees in mechanical engineering from the University of Michigan, Ann Arbor, in 1998 and 2001, respectively. He is currently a Professor in mechanical engineering with the Ulsan National Institute of Science and Technology (UNIST), South Korea.

From 2001 to 2003, he was a Postdoctoral Research Fellow with the University of Michigan. From 2003 to 2008, he was an Assistant Professor of mechanical engineering at Michigan State University, East Lansing, MI, USA. His research interests include laser material interaction and processing, multiphysics simulations, and deep-learning applications.

• • •